

# Two-Staged Rupture of the 19 October 2020 $M_w$ 7.6 Strike-Slip Earthquake Illuminated the Boundary of Coupling Variation in the Shumagin Islands, Alaska

Zhifan Wan<sup>1</sup>, Dun Wang<sup>\*1</sup>, Junfeng Zhang<sup>2</sup>, Qi Li<sup>3</sup>, Lianfeng Zhao<sup>4</sup>, Yifang Cheng<sup>5</sup>, Jim Mori<sup>6</sup>, Fang Chen<sup>1</sup>, and Yuyang Peng<sup>1</sup>

## Abstract

On 19 October 2020, an  $M_w$  7.6 earthquake occurred within the Shumagin Islands, Alaska, which is the largest strike-slip earthquake occurred in the shallow subducted plates with abundant seismic observations. Here, we relocated the earthquake sequence, implemented back-projection analyses, and finite-fault inversion to investigate the source processes of the mainshock, and calculated mainshock focal mechanisms using the polarities of  $P$  waves and  $W$ -phase inversion, respectively. Our results show that the faulting of the mainshock can be divided into two segments with the initial rupture along a steep plane (strike =  $15^\circ$ , dip =  $81^\circ$ ) and propagation southeastward along a more shallowly dipping plane (strike =  $344^\circ$ , dip =  $48^\circ$ ). The inferred strikes of the mainshock faults are similar to the orientations of preexisting structures in the source region, likely indicating that the 2020  $M_w$  7.6 earthquake ruptured along the preexisting plate fabric in the down-going plate. The fabrics are located at the boundary with significant variations of the plate coupling, indicating that these structures within the subducting plate may affect the interplate coupling or as a result of the varying interplate coupling in subduction zones.

**Cite this article as** Wan, Z., D. Wang, J. Zhang, Q. Li, L. Zhao, Y. Cheng, J. Mori, F. Chen, and Y. Peng (2022). Two-Staged Rupture of the 19 October 2020  $M_w$  7.6 Strike-Slip Earthquake Illuminated the Boundary of Coupling Variation in the Shumagin Islands, Alaska, *Seismol. Res. Lett.* **94**, 52–65, doi: [10.1785/SRL20220203](https://doi.org/10.1785/SRL20220203).

[Supplemental Material](#)

## Introduction

The Shumagin gap had been identified as the region of a potential megathrust earthquake in the Shumagin Islands, Alaska (Sykes, 1971; Davies *et al.*, 1981), which was between the ruptured areas of the 1938  $M_w$  8.2 and the 1942  $M_w$  8.6 earthquakes. Based on seismicity and geodetic observations, it was inferred that the Shumagin gap was under low plate interplate coupling and unlikely to host a great earthquake (Fletcher *et al.*, 2001; Cross and Freymueller, 2008). From July 2020 to August 2021, three large earthquakes with  $M_w > 7.5$  occurred in the vicinity of the Shumagin Islands. The  $M_w$  7.8 thrust earthquake occurring on 22 July 2020 was a subduction interface earthquake that ruptured from the eastern Shumagin gap to the northwest (Crowell and Melgar, 2020; Shillington *et al.*, 2020; Ye *et al.*, 2021). On 19 October 2020, an  $M_w$  7.6 intraplate strike-slip earthquake occurred within the subducting plate. On 29 July 2021, an  $M_w$  8.2 thrust faulting earthquake occurred along the subduction interface and ruptured eastward from the hypocenter (Fig. 1). This study focuses on the second largest event of the sequence—the strike-slip earthquake of the 19 October 2020, which is the largest intraplate strike-slip earthquake in shallow subducted plates with rich seismic observations.

Previous studies suggested that large oceanic intraplate earthquakes often ruptured along preexisting geological structures (e.g., Meng *et al.*, 2012; Satriano *et al.*, 2012; Wang *et al.*, 2012; Herman *et al.*, 2014; Krabbenhoef *et al.*, 2018, 2021; Jacob *et al.*, 2021). For example, based on seismicity, marine seismic reflection profiling and heat flow observations, the intraplate strike-slip earthquakes in the northeastern Indian ocean were interpreted as the activation of preexisting fractures along the Ninety East ridge (Weissel *et al.*, 1980), which was further verified by multichannel seismic reflection profiles and

1. Badong National Observation and Research Station of Geohazards, School of Earth Sciences, China University of Geosciences, Wuhan, China,  <https://orcid.org/0000-0002-0440-6054> (ZW);  <https://orcid.org/0000-0003-4512-3103> (YP); 2. State Key Laboratory of Geological Processes and Mineral Resources, School of Earth Sciences, China University of Geosciences, Wuhan, China,  <https://orcid.org/0000-0002-2834-2833> (JZ); 3. Key Laboratory of Earthquake Geodesy, Institute of Seismology, China Earthquake Administration, Wuhan, China; 4. Key Laboratory of Earth and Planetary Physics, Institute of Geology and Geophysics, Chinese Academy of Sciences, Beijing, China,  <https://orcid.org/0000-0002-1400-3064> (LZ); 5. Department of Earth Sciences, University of Southern California, Los Angeles, California, U.S.A.,  <https://orcid.org/0000-0002-6507-5607> (YC); 6. Disaster Prevention Research Institute, Kyoto University, Uji, Japan

\*Corresponding author: wangdun@cug.edu.cn

© Seismological Society of America

focal mechanisms (Bull and Scrutton, 1990; Karner *et al.*, 1993). Relocations and focal mechanisms for the earthquakes in the region of the southwest Pacific Ocean, suggested that those earthquakes were attributed to the activation of a fossil fracture at the Macquarie ridge complex (Valenzuela and Wysession, 1993).

In the source area of the 2020  $M_w$  7.6 earthquake, there are north-south-oriented fracture zones from the Vancouver-Pacific spreading near the Shumagin gap (Naugler and Wageman, 1973; Atwater, 1989); slight variations in the strikes of the magnetic anomalies were observed in areas adjacent to the source region of the  $M_w$  7.6 Alaska earthquake (Naugler and Wageman, 1973). Thus, a north-northwest-striking fault plane was utilized in the finite-fault inversion and successfully modeled the seismic observations (The U.S. Geological Survey [USGS]; Jiang *et al.*, 2022; Zhou *et al.*, 2022). Stress modeling indicated that the July  $M_w$  7.8 thrust event and its afterslip helped to trigger the October  $M_w$  7.6 event, assuming that the Shumagin gap was less coupled (Herman and Furlong, 2021; Jiang *et al.*, 2022).

To investigate the source characteristics and the local seismogenic structures, we relocated the earthquake sequence, calculated the focal mechanism of the mainshock, and carried out back-projection analyses for the mainshock. The results indicated that the rupture process of the 2020  $M_w$  7.6 Alaska earthquake had two distinct parts. The earthquake first ruptured southwestward  $\sim 16$  km along a steep fault plane for the first 16 s; then the rupture propagated southeastward  $\sim 42$  km along a moderately dipping plane from 17 to 26 s after the origin time. The strikes of the ruptured faults correlated well with the orientations of the linear magnetic anomalies in the source area. The 2020  $M_w$  7.6 Alaska earthquake and other  $M_w > 5.5$  intraplate strike-slip earthquakes since 1990 in this region are located in areas with significant variations of coupling rates, which delineated the boundary of the coupling changes.

## Relocation of the Earthquake Sequence

According to the earthquake catalog of the USGS, there were more than 2685 aftershocks in the three months following the mainshock, including 121  $M \geq 4.1$ , 462  $M$  3.1–4.0, 1720  $M$  2.1–3.0, and 382  $M$  2.1–3.0 events. The  $b$ -value for the Gutenberg-Richter law was 0.76 (Fig. 1a), which is consistent with the background  $b$ -value in the Shumagin Islands (Liu *et al.*, 2020).

We applied a relative relocation algorithm to determine the locations of all 121  $M_w \geq 4.1$  aftershocks, using seismic data recorded mainly in the Gulf of Alaska and western Canada, including  $\sim 350$  broadband stations with the epicentral distances from about  $5^\circ$ – $20^\circ$  (Fig. 2a). We relocated the earthquakes using the arrival time differences of the  $Pn$  waves at all stations calculated by waveform cross correlation (Zhao *et al.*, 2016; Guo *et al.*, 2017; Wang and Hutko, 2018). We first set the grid points with 0.5 km spacing at 28.4 km depth (focal depth determined by the USGS) for the potential source locations. Then, we aligned the waveforms of a reference and target earthquakes

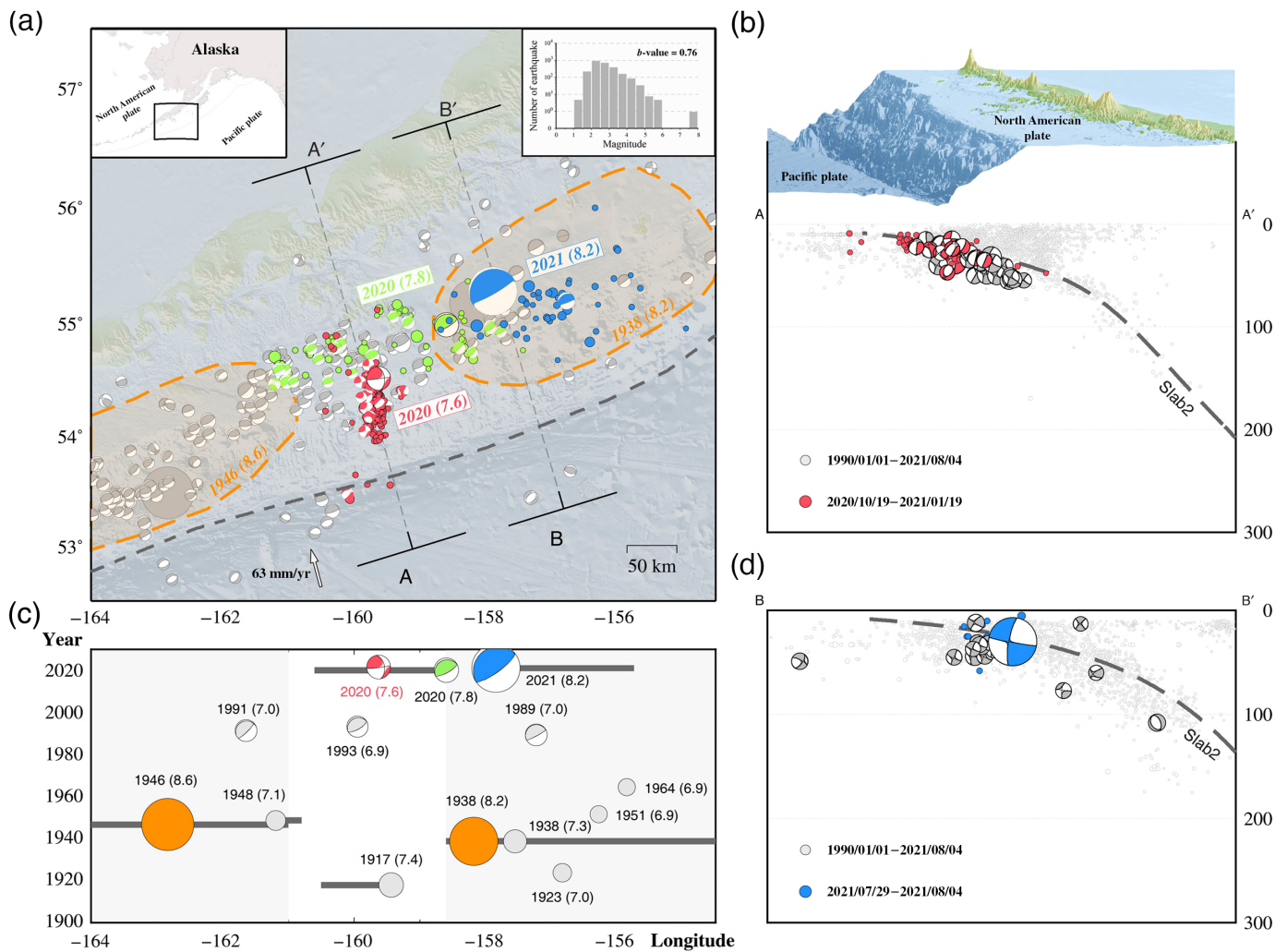
by the cross-correlation technique using a three-second window with a two-second offset followed by the manual check. The origin time of the target earthquakes was designated within  $\pm 2$  s relative to its origin time in the USGS catalog. Next, we eliminated the station pairs of earthquakes with cross-correlation coefficients  $\leq 0.5$  to remove the noisy data. We searched for the best location and origin time of the target earthquake by minimizing the travel-time residuals (Wang and Mori, 2012). This method has a high horizontal resolution but without depth resolution.

We selected an  $M_w$  5.1 earthquake that occurred in the northern portion of the rupture region as the reference event. The distribution of the relocated aftershocks suggested two segments for the mainshock. The aftershocks in the north (close to the epicenter) appear to be linearly distributed along a narrow north-northeast-striking fault. Although the source depths of the earthquakes were not relocated, the relocated earthquakes in the north (cross section A–A' of Fig. 2d) still suggested a steeply dipping fault plane. In the south, the aftershock distribution inferred a north-northwest-striking fault with a relatively moderate dip angle. To evaluate the possible location bias in the relocation analysis, we calculated the location uncertainties by assuming laterally homogenous structure, and using  $Pn$  velocities at 7.6 and 8.3 km/s. The average value of the travel-time residuals ( $\sim 0.5$  s) indicated a horizontal location uncertainty of  $\sim 4$  km (Fig. S1, available in the supplemental material to this article). To check the potential bias caused by the selected reference event, we selected another  $M_w$  5.1 event in the southern part of the source region and relocated the earthquake sequence. The general features of the results derived from the relative relocations using different reference events were similar, implying two segments for the mainshock rupture, likely a north-northeast-striking fault plane with a steeply dipping angle in the north and a north-northwest-striking fault plane with a moderately dipping angle in the south (Fig. 2; Table S1).

## Back Projections

High-frequency  $P$  waves are likely radiated from rupture front of large earthquakes. Therefore, back projection of high-frequency  $P$  waves could track the rupture propagation and source duration (Zhang and Ge, 2010; Koper *et al.*, 2012; Yao *et al.*, 2012; Vallée and Satriano, 2014; Fan and Shearer, 2017; Huang *et al.*, 2022); therefore, it can image the fault geometry of large earthquakes in high resolution (Ishii *et al.*, 2005). Here, we back-projected the seismograms recorded at the Global Seismographic Network (GSN) (filtered between 0.6 and 5.0 Hz) and the China array (filtered between 1.0 and 5.0 Hz) (Zheng *et al.*, 2010). A total number of 92 GSN stations with epicentral distances of  $30^\circ$ – $90^\circ$  and 829 Chinese stations with epicentral distances of  $40^\circ$ – $81^\circ$  were used.

The horizontal grid of  $100 \times 100$  points was set up with a 2 km spacing at 28.4 km depth. Numerous investigations have shown that the fixed depth has a little impact on the horizontal

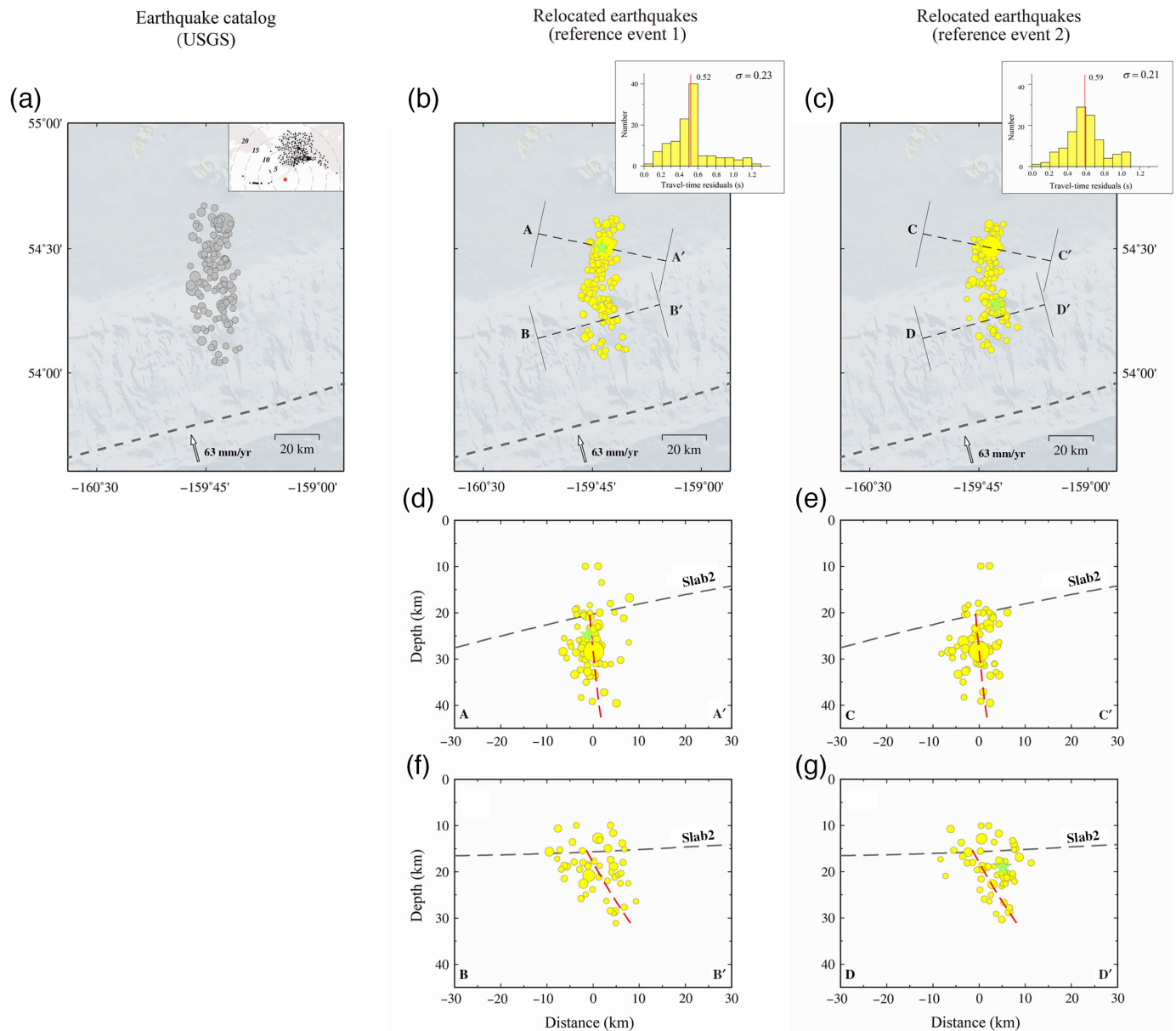


resolution of the back projection (e.g., Kiser and Ishii, 2012; Yao *et al.*, 2012; Wang *et al.*, 2018). Then, using the Earth model International Association of Seismology and the Physics of the Earth's Interior, 1991 (IASPEI91) (Kennett and Engdahl, 1991), we determined the travel times between the stations and the grid points, and we aligned the filtered waveforms (0.05–0.5 Hz) using a 30 s window with an 8 s offset by cross correlation. After using the time offset obtained in the first cross-correlation calculation, we cross-correlated the filtered data (0.6–5.0 Hz for GSN and 1.0–5.0 Hz for China array) with a 6 s window and allowing 1 s offset. Finally, the most likely source locations were derived from the locations of points with the largest stack amplitude in each time window.

The results of the back projections showed that the rupture lasted  $\sim 26$  s (Fig. 3). The rupture initiated with a relatively slow rupture speed of 1 km/s in the first 16 s, then changed direction, and ruptured  $\sim 42$  km with a speed of 4.2 km/s. This speed is faster than the local shear-wave velocity at the depth of 28.4 km (4.0 km/s, according to Pasyanos *et al.*, 2014), indicating a potential supershear rupture, despite the marginally supershear speed. The results derived from the GSN and China array showed similar rupture patterns, although there

**Figure 1.** Seismicity in and around the Shumagin Islands region. (a) Locations and focal mechanisms of the earthquakes from 1976 to 2021 (Global Centroid Moment Tensor [Global CMT]). The focal mechanisms of the earthquake sequences before the July 2020, of the 2020  $M_w$  7.8, 2020  $M_w$  7.6, and 2021  $M_w$  8.2 earthquakes are plotted in gray, green, red, and blue respectively, with circle sizes scaled by magnitude. The rupture regions of the 1938 and 1946 earthquakes are delineated by the dashed orange lines according to Benz *et al.* (2011). The top-right inset shows the magnitude–frequency relationship and the corresponding  $b$ -value for the  $M_w$  7.6 earthquake sequence. (c) Time sequence of large historical earthquakes ( $M_w > 6.9$ ) and their rupture extents along longitude (Estabrook and Boyd, 1992; Liu *et al.*, 2020). The segment labeled in white was termed the Shumagin gap. (b, d) Cross sections A–A' and B–B' in a width of 50 km. Gray circle indicates historical earthquakes before the  $M_w$  7.6 earthquake sequence. The red and blue circles represent the locations of the  $M_w$  7.6 and 8.2 earthquake sequences, respectively. The gray dashed lines show the slab surface of Slab2 (Hayes *et al.*, 2018). The color version of this figure is available only in the electronic edition.

were some differences in the locations of the southern portion, which could be attributed to the uncertainties in the back projection due to differences in azimuthal coverage. To assess the



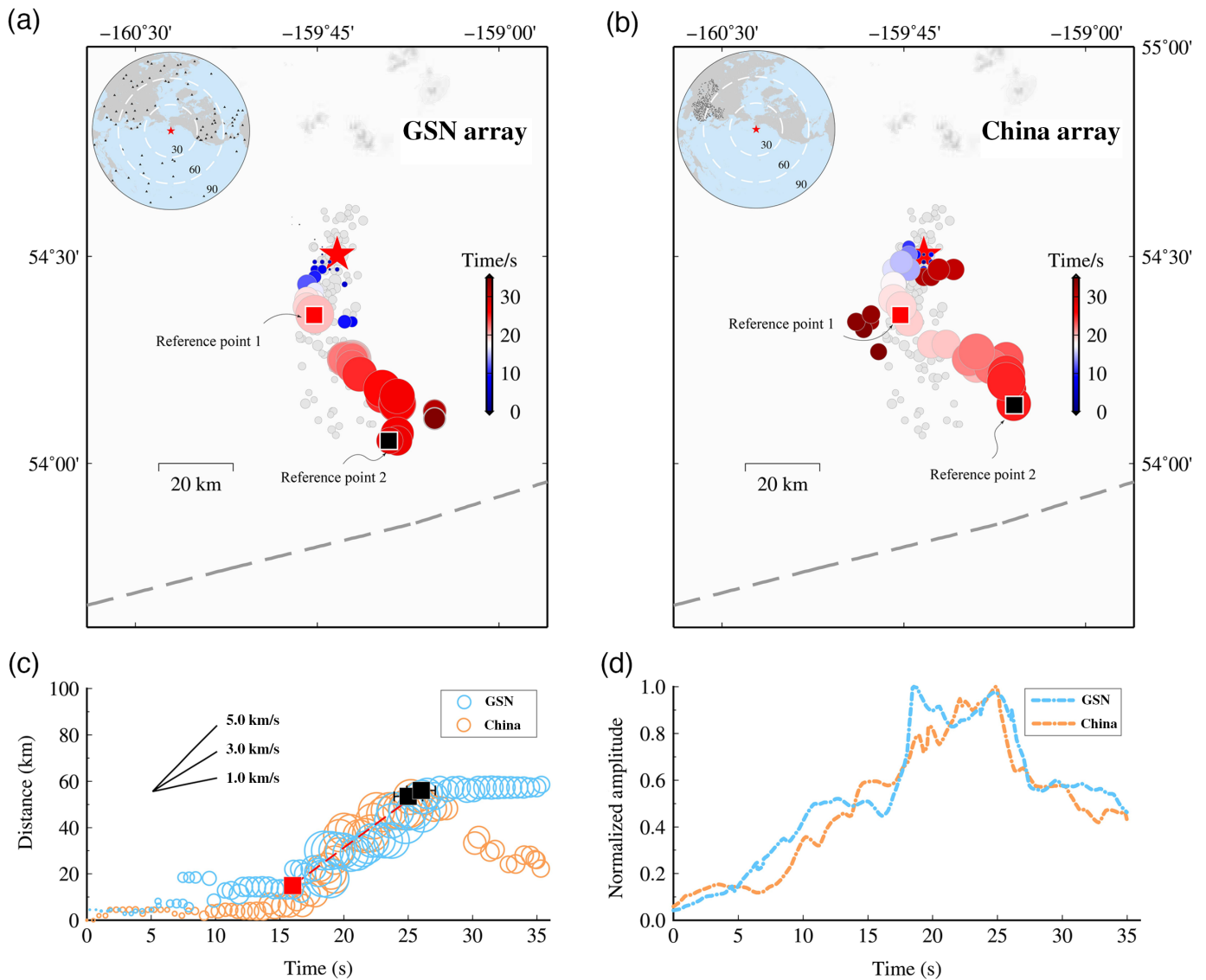
location uncertainties in the back-projection analyses, we back-projected five  $M_w \geq 5.5$  moderate aftershocks. The station corrections derived from the mainshock were applied to analyze these smaller events (Wang *et al.*, 2018). There were small differences of approximately 10–20 km between the back-projection locations of the five aftershocks and the USGS or Global Centroid Moment Tensor (Global CMT) locations. Therefore, the average uncertainties of absolute locations in our back-projection results were around 10–20 km (Fig. 4).

## Rupture Process from Finite-Fault Inversion

### Focal mechanisms

We calculated the focal mechanism of the mainshock using the first-motion data observed at the vertical components of global stations (Fig. S2a) following the algorithm of Hardebeck and Shearer (2002). First, we identified the  $P$ -wave first-motion

**Figure 2.** Locations of the original and relocated earthquake sequences ( $M_w > 4.1$ ) that occurred within three months following the mainshock. The gray dashed line represents the trench. (a) Locations of the  $M_w > 4.1$  earthquakes according to the U.S. Geological Survey (USGS) catalog. (b) Location of the relocated earthquake sequence using an  $M_w$  5.1 earthquake in the north as the reference event (green star). Inset exhibits the results of travel-time residuals and the standard deviations with the mean value represented by the red line. (c) The same as in panel (b) except that the reference event is an  $M_w$  5.1 earthquake in the south (green star). (d,f) Cross sections of the earthquake sequence along cross sections A–A' and B–B', respectively. The red dashed lines in panels (d) and (f) represent the dip angles of inferred fault planes derived from the focal mechanisms of  $P$ -wave first motion and  $W$ -phase inversion, respectively. (e,g) The same as panels (d) and (f) but for the cross sections C–C' and D–D'. The color version of this figure is available only in the electronic edition.



polarity on the unfiltered vertical components of 928 seismic stations with epicentral distances of up to  $85^\circ$ . We calculated the takeoff angles for each station, and then utilized the grid search to locate all acceptable solutions (the number of misfit polarities less than 8). The preferred focal mechanism solution was further selected according to the root-mean-square angular difference among all the acceptable focal mechanisms. Those preferred focal mechanism solutions were averaged to form the final focal mechanism. Similar to the default setting in Hardebeck and Shearer (2002), we included all the acceptable focal mechanism solutions to form the final focal mechanism. We utilized two different velocity models (preliminary reference earth model [Dziewonski and Anderson, 1981] and IASPEI91 [Kennett and Engdahl, 1991]) in calculating the takeoff angles, but the estimated focal mechanisms did not show observable differences.

The obtained *P*-wave first-motion solution represented the focal mechanism of the initial rupture of the mainshock ( $15^\circ/81^\circ/137^\circ$  for strike/dip/rake). The focal mechanism derived

**Figure 3.** Source process of the 2020  $M_w$  7.6 Alaska earthquake imaged by back-projecting seismograms recorded at (a) Global Seismographic Network (GSN) and (b) Chinese stations. The red star represents the location of the mainshock epicenter. Gray circles represent the locations of relocated aftershocks (Fig. 2b). The inset represents the seismic stations included in the back projections. (c) Time–distance plots of the back-projection results. The distances are calculated from the epicenter (red star) except for the southeastward rupture that started 16 s after the origin time, in which a reference point (red square) is given for calculating the rupture propagation distance. The black square indicates the end position of the second segment. The red dashed lines indicate the average speed for the rupture after 16 s. (d) Normalized maximum amplitude estimated from each time window as a function of time. The color version of this figure is available only in the electronic edition.

from the *W*-phase inversion in this study ( $344^\circ/48^\circ/171^\circ$  for strike/dip/rake) was different from the *P*-wave first-motion solution but consistent with the centroid mechanisms determined



by the Global CMT ( $350^{\circ}/46^{\circ}/176^{\circ}$  for strike/dip/rake) and USGS ( $350^{\circ}/49^{\circ}/173^{\circ}$  for strike/dip/rake). The clear difference between the two types of focal mechanisms showed the complexity of the rupture process, indicating that the focal mechanism of the mainshock varied during the rupture process (Fig. 5). Another evidence that indicated the source complexity is the relatively large non-double-couple component (29%) shown in the focal mechanism solution of the *W*-phase inversion (USGS).

The strike and dip angles of the rupture plane ( $15^{\circ}/81^{\circ}/137^{\circ}$  for strike/dip/rake) derived from the *P*-wave polarities were consistent with the orientation of the north segment delineated by the relocated aftershocks and back projection. The strike and dip angles of the fault plane from the *W*-phase inversion ( $344^{\circ}/48^{\circ}/171^{\circ}$  for strike/dip/rake in this study) were consistent with the orientation of the south segment of the fault plane, as shown by the relocated aftershocks and back projection. In addition, both the back-projection results of the GSN and China arrays showed that the large seismic energy was radiated from the second segment (Fig. 3d). Hence, we used the focal mechanism of the *W*-phase inversion as the focal mechanism of the second segment in the following finite-fault modeling.

**Figure 4.** Back-projection results for five  $M_w > 5.5$  earthquakes using station corrections derived from the mainshock. The triangle and inverted triangle represent the locations of the maximum stacked amplitudes of the aftershocks derived from back projections using Chinese and global seismic data, respectively. The octagon, pentagon, diamond, and square indicate the epicenters determined by the USGS, Global CMT, and relocated locations using reference event 1 and reference event 2, respectively. Available focal mechanisms are plotted from the Global CMT (red) and the USGS (blue). The color version of this figure is available only in the electronic edition.

In summary, the rupture of the mainshock consisted of two stages. For the first stage, the earthquake ruptured along a steep (dip angle  $81^{\circ}$ ) rupture plane with a strike of  $15^{\circ}$ , according to the focal mechanism of the *P*-wave polarities. In the second stage, the rupture propagated southeast along a moderate dipping (dip angle  $48^{\circ}$ ) fault plane with a strike of  $344^{\circ}$  according to the *W*-phase inversion. The two-staged rupture process was verified by the back-projection analyses and relocations of the aftershocks.

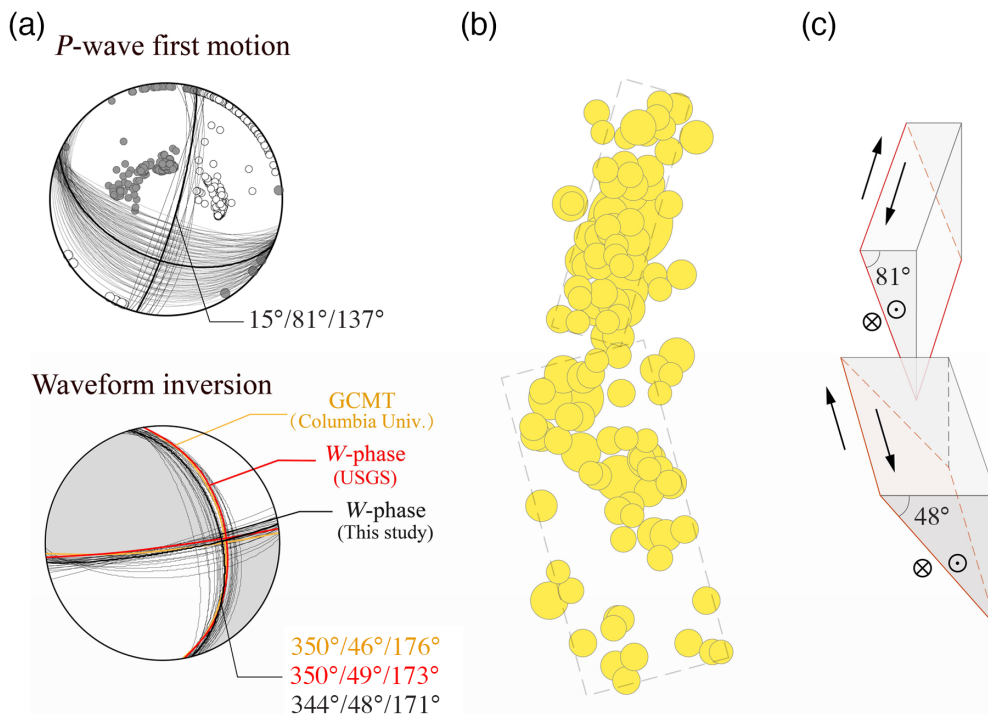


**Figure 5.** Geometries of the fault planes of the 2020  $M_w$  7.6 Alaska earthquake delineated by focal mechanisms and the relocated aftershocks. (a) The focal mechanisms of  $P$ -wave polarities and waveform inversions (Global CMT [see [Data and Resources](#)],  $W$  phase from the USGS, and  $W$  phase in this study); the uncertainties were plotted by gray lines on the  $P$ -wave first-motion mechanism and  $W$ -phase solution. The clear difference between the focal mechanisms of the  $P$ -wave polarities and waveform inversion indicated the varying focal mechanism during the rupture process. (b) The distribution of the relocated aftershocks shown in Figure 2b, in which two faults are inferred (gray dashed rectangle). (c) A two-fault rupture model for the earthquake. The color version of this figure is available only in the electronic edition.

## Slip inversion

We downloaded  $P$  waveforms recorded at 52 GSN broadband stations with epicentral distances in the range of  $30^\circ$ – $90^\circ$  from the Incorporated Research Institutions for Seismology. We first removed the instrument response, converted the data to displacement, and then filtered them with a band-pass filter of 0.01–0.5 Hz with a 0.5 s sampling interval. Next, we used a kinematic source inversion package (MudPy) to model the slip distribution along the fault planes (Crowell and Melgar, 2020; Li *et al.*, 2020; Xiao *et al.*, 2022). The inversion of the source rupture slip distribution can be simplified to a linear problem in time domain, and the inversion process seeks to minimize the fit of the observed slips and the roughness of the slip distribution:

$$\text{minimum} \|w(\mathbf{G} \cdot \mathbf{M} - \mathbf{D})\|^2 + \beta^2 \|\mathbf{L} \cdot \mathbf{M}\|^2, \quad (1)$$

in which  $w$  represents the weight, centered dots represent dot product, and  $\mathbf{D}$  represents the observed waveforms;  $\mathbf{L}$  is the Laplace operator;  $\mathbf{M}$  represents the slip amount or seismic moment, which is the quantity to be determined, and the variable

slip angle can be estimated by two slip vectors (slip angle  $\pm 45^\circ$ );  $\mathbf{G}$  represents the Green's function, and the far-field  $P$ -wave Green's function is calculated by the QSSP algorithm (Wang *et al.*, 2017). The value of the smoothing factor  $\beta$  is determined by the trade-off curve showing the model roughness and the residual. A nonnegative least-squares algorithm (Lawson and Hanson, 1995) is used to calculate the amount of slip on each sub-fault.

Based on the analyses in focal mechanisms of the main-shock, we set up a two-fault model to implement the finite-fault modeling for the  $M_w$  7.6 earthquake. Fault 1 (strike  $15^\circ$ , dip  $81^\circ$ ) was set as  $32 \text{ km} \times 33 \text{ km}$  and was divided into  $8 \times 11$  subfaults along the strike and dip directions, respectively. Fault 2 (strike  $344^\circ$ , dip  $48^\circ$ ) was set as  $48 \text{ km} \times 30 \text{ km}$  and was divided into  $12 \times 10$  subfaults along the strike and dip directions, respectively. For each

subfault, we parameterized the source by three triangle functions with a duration of 3 s for each and separated by 1.5 s. The optimal smoothing factor in this study is set as 0.13 (Fig. S3).

To estimate the rupture speeds of the entire rupture and evaluate their influence in the finite-fault modeling, a series of rupture speeds for both the northern and southern segments were utilized (Fig. 6). Inversions assuming rupture speeds of 1.0 and 4.0 km/s for the first and second segments and a rupture speed of 2.0 km/s for the first and second segments fitted the observations almost equally well (Fig. 6; Figs. S4–S6). However, results from the back projection of global and Chinese stations supported the first scenario (Fig. 3). Considering the rupture speeds estimated by the back projections, the slip model with the varying speeds of 1.0 and 4.0 km/s were favored.

Results of finite-fault modeling with rupture speeds of 1.0 and 4.0 km/s for the first and second segments indicated that the earthquake started from the north–northeast-striking fault and released  $\sim 30\%$  of the total seismic moment in the first 15 s, which was shown as the first peak in the source-time function (Fig. 7b). The majority of the moment was released

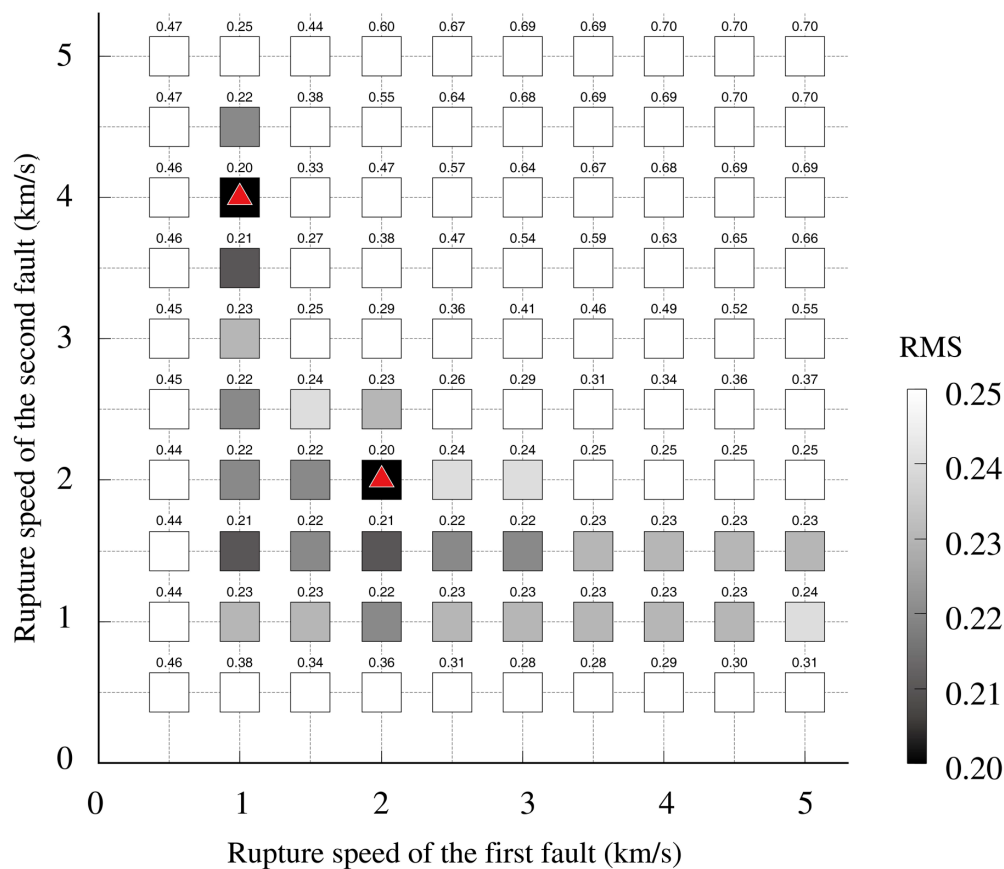


**Figure 6.** Residuals between observed and synthetic waveforms for a range of rupture speeds for the two segments of the ruptures during the 19 October 2020  $M_w$  7.6 Alaska earthquake. Red triangle indicates the locations of the minimum residuals. The RMS is the residual displacements between the observations and synthetics. The color version of this figure is available only in the electronic edition.

from 16 to 25 s, indicating that the radiated energy of the earthquake was predominantly produced in the second segment (north–northwest-striking fault), thereby explaining why the focal mechanisms derived from waveform inversions (USGS and Global CMT) were more consistent with the second fault. The slip that occurred on the south segment was mainly strike-slip motion, and the maximum slip was  $\sim 6.0$  m at  $\sim 30$  km depth (Fig. 7c), which was almost the bottom of the aftershock zone. There were two possible explanations for this point. The first possible reason was that the locations of the aftershocks and the mainshock slips were complimentary to each other. It was frequently seen in many large earthquakes. Another possible reason was that the depths of the aftershocks might be biased in the original earthquake catalog by the USGS, because there were not many close seismic stations for the offshore earthquakes. The total source duration was  $\sim 25$  s, which generally matched the results of the back projections. This two-fault model showed a 32% non-double-couple component, comparable to the value of 29% shown in the solution in the  $W$ -phase inversion by the USGS.

To evaluate the uncertainty of the inverted slips in the finite-fault inversion, we randomly selected 80% of the total seismic stations (Fig. 7a) to perform inversion and repeated the inversion 1000 times. The standard deviation of the slip model was  $\sim 0.10$  m, as shown in Figure S7.

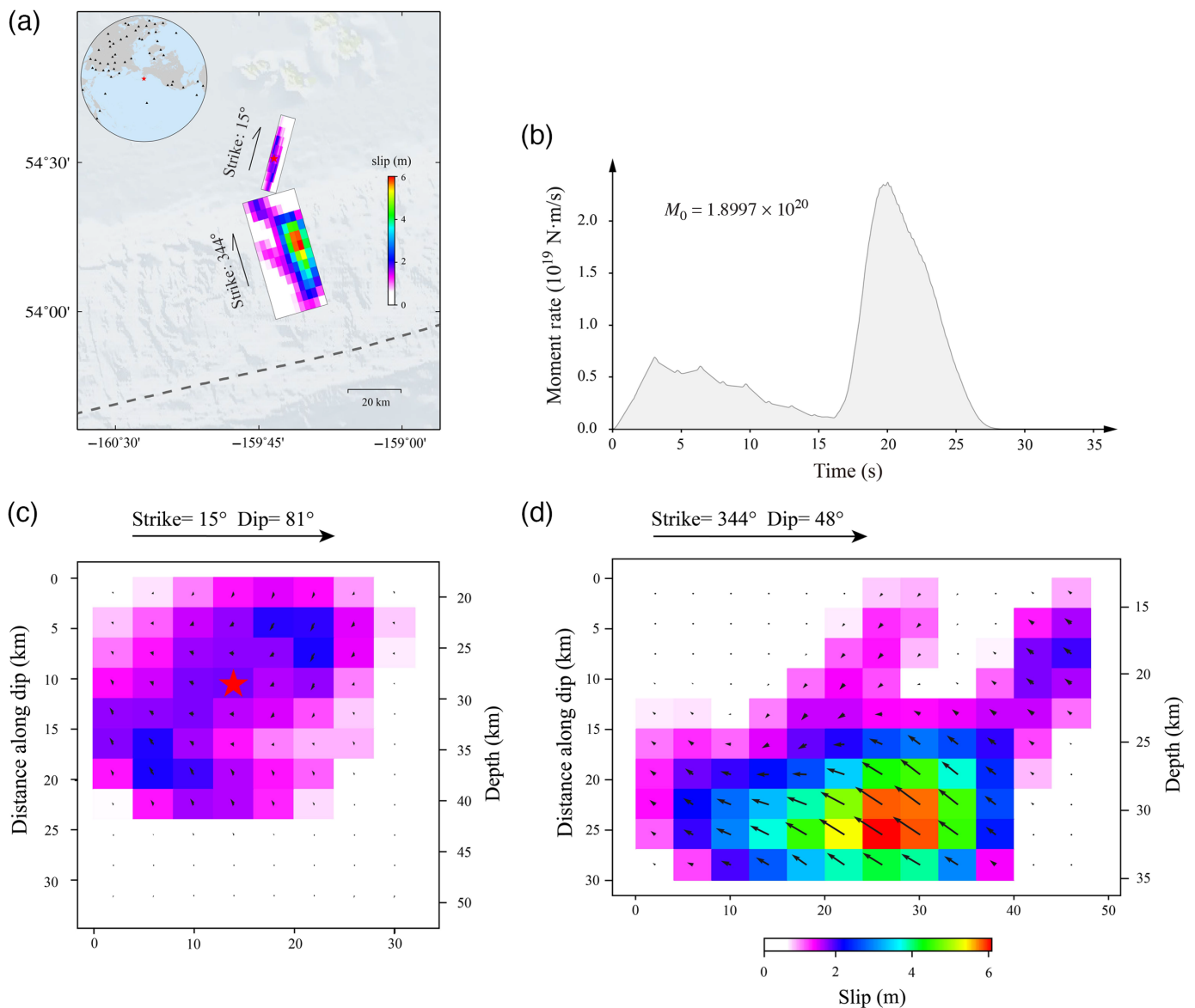
## Discussion

### Correlation between intraplate earthquakes and preexisting seafloor fabrics

Although the correlation between intraplate strike-slip earthquakes within the subducted plates and preexisting seafloor fabrics was suggested in several cases (e.g., [Satriano et al., 2012](#); [Song et al., 2019](#); [Jacob et al., 2021](#); [Krabbenhoft et al., 2021](#)), it is still unclear how this correlation is solid due to limited seismic observations. The 2020  $M_w$  7.6 Alaska strike-slip event is the biggest strike-slip earthquake that occurred in the shallow portion of the downgoing plate with

abundant seismic observations. For this earthquake, a north–northwest-striking preexisting plate fabric was suggested and used as the fault plane to model the seismological and geodetic observations ([Jiang et al., 2022](#); [Zhou et al., 2022](#); USGS). However, the fine process of the source process and its correlation to the previous fabrics was not comprehensively investigated.

With rich local, regional, and global observations, we were able to observe the rupture pattern in unprecedented resolution. The detailed two-stage rupture pattern showed very similar characteristics of the seafloor fabrics in and around the source region (Fig. 8b). If the ruptured faults of the earthquake were related to preexisting seafloor fabrics, the strikes and dips of the fabrics can be restored back to the unsubducted status by considering the dip angles of the subducted plate interface and the geometry of the ruptured faults using a stereographic projection ([Coxeter, 1969](#)). Using the strike and dip angles of the subducted plate ( $237.7^\circ/14.5^\circ$  for strike/dip from Slab2), we restored the orientations of the north and south segments of the rupture faults to the oceanic plate, which were  $185^\circ/88^\circ$  and  $355^\circ/53^\circ$ , respectively (Fig. 8a). The restored strikes of the ruptured faults were consistent with the orientations of



the magnetic anomalies, and such bent characteristics of the plate fabric is very similar to those of the restored two-staged fault planes.

A similar pattern of two-stage rupture was also seen in the 1999  $M_w$  7.0 strike-slip earthquake, Kodiak Island, as inferred from the difference of focal mechanisms derived from the  $P$ -wave first-motion mechanisms and the  $W$ -phase inversion (Fig. 8c; Hansen and Ratchkovski, 2001; Ratchkovski and Hansen, 2001). The two strikes of the rupture segments for the 1999 event were similar to the strikes of the two-stage rupture found in this study for the 19 October 2020 event.

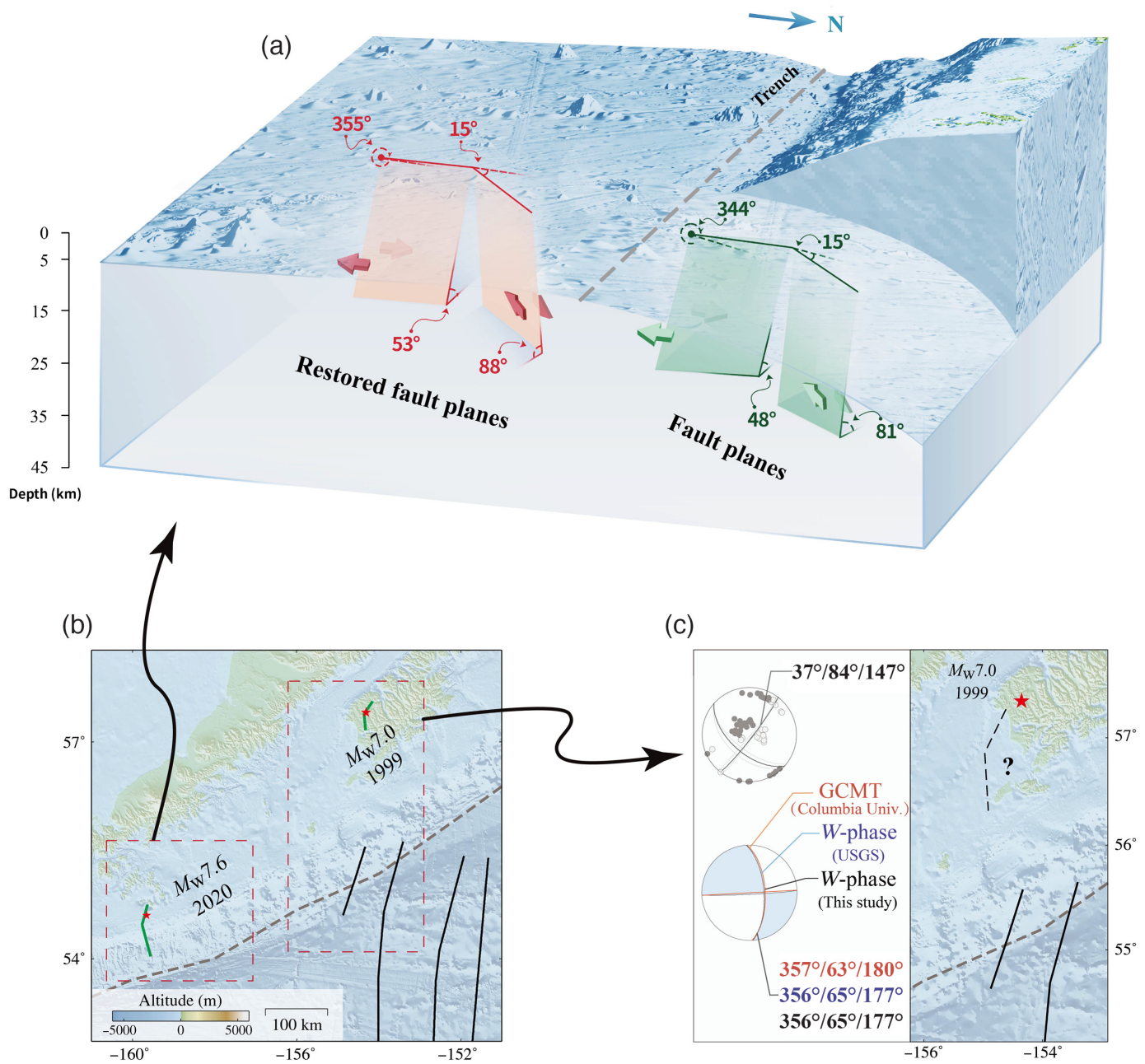
Stress modeling in the Shumagin Island suggested that a north–south-oriented preexisting fabric was favored to generate the  $M_w$  7.6 earthquake, because the stress field across the coupled and weakly coupled boundary may not be sufficient to cause an  $M_w$  7.6 earthquake without an existing host fault (Herman and Furlong, 2021). Therefore, we suggest that both the 1999 Kodiak earthquake and the 19 October 2020

**Figure 7.** Finite-fault inversion for the 19 October 2020  $M_w$  7.6 Alaska earthquake with rupture speeds of 1.0 and 4.0 km/s for the north and south segments, respectively. (a) Distribution of the inverted slip in map view. Inset shows the locations of the utilized seismic stations (black triangle). (b) The source-time function for the slip model. (c) Distribution of the inverted slip on the two fault planes. The color version of this figure is available only in the electronic edition.

earthquake in this study are related to the activation or reactivation of the plate fabric of the magnetic anomalies.

### Subducted plate fabrics and interplate coupling

There are many along-strike variations in seismicity and coupling in subduction zone. Understanding the physical mechanism of along-strike variations of plate coupling is important for the seismic hazard and related hazards such as tsunamis. The thickness and lithology of sediments, dehydration of



sediments, and the fluids on the interface are associated with the coupling process and seismic behavior at various active convergent margins such as Costa Rica, northern Japan, and Hikurangi (e.g., Saffer and Tobin, 2011; Sun *et al.*, 2020). Also, the variation of fault geometry and large topographic features (such as seamounts) in the Nankai subduction zone was suggested to contribute to the varied interplate coupling (Yokota *et al.*, 2016; Tsuji *et al.*, 2017).

Coupling variation in the Alaska–Aleutian subduction zone showed a gradient from the highly coupled rupture area of the 1938  $M_w$  8.2 earthquake to a less coupled Shumagin gap according to the dense Global Positioning System (GPS) observations (Fournier and Freymueller, 2007). Comparing the locations between the intraplate earthquakes and the boundaries of

**Figure 8.** Location correlations of the ruptured faults with the linear magnetic anomalies. (a) Transparent green rectangles indicate the inferred geometries of the ruptured faults for the 2020  $M_w$  7.6 Alaska earthquake. Those fault planes were then restored to the unsubducted status by a stereographic projection (Coxeter, 1969), which is shown by the transparent red rectangles. (b) The heavy solid lines indicate the magnetic lineation (Naugler and Wageman, 1973). The red stars represent the epicenters of the 1999  $M_w$  7.0 and 2020  $M_w$  7.6 earthquakes. The geometries of the two fault planes are represented by green solid lines. (c) Focal mechanisms of the 1999  $M_w$  7.0 Kodiak Island earthquake derived from the  $P$ -wave first motions and waveform inversions. GCMT, Global CMT. The color version of this figure is available only in the electronic edition.

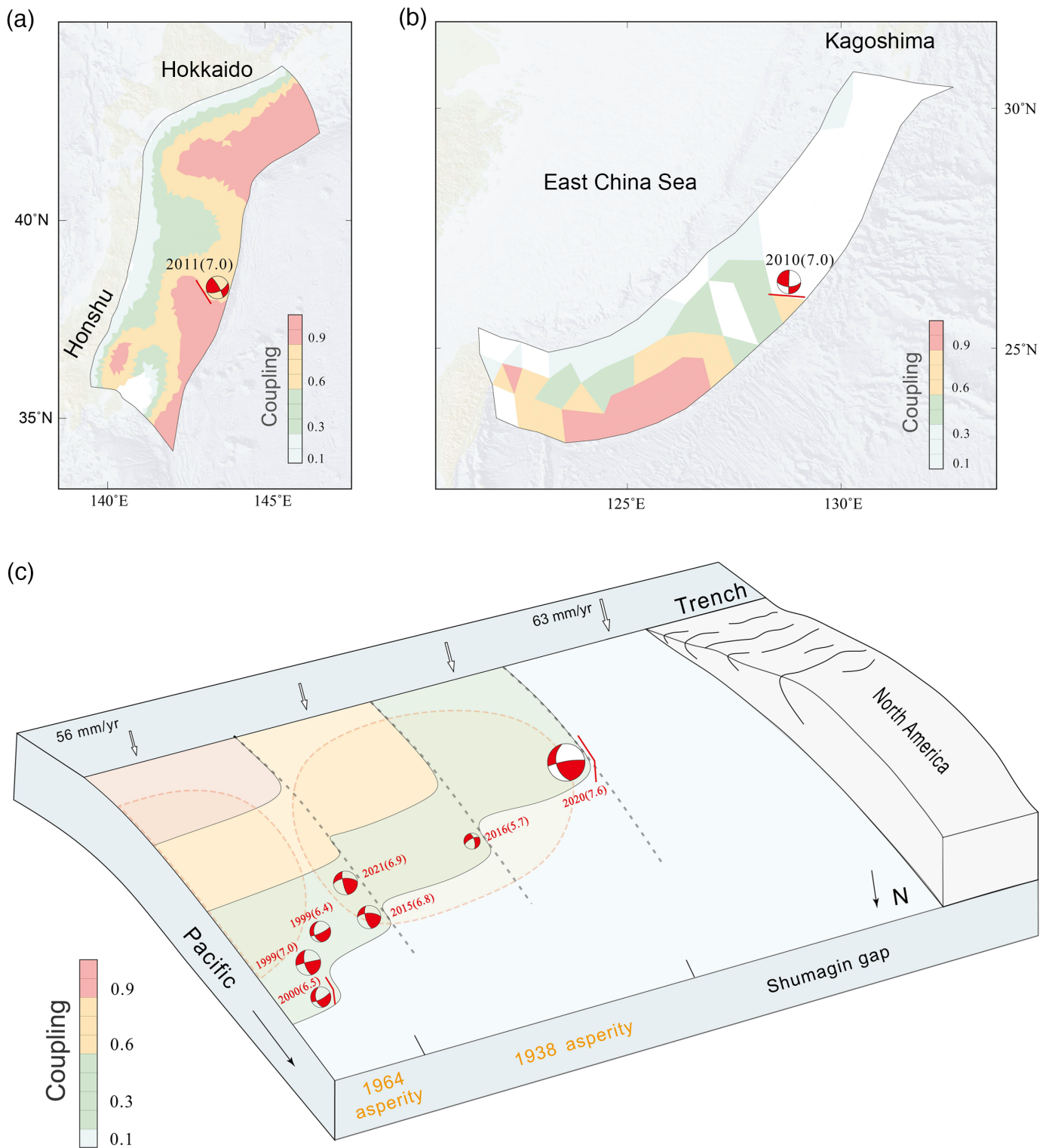


**Figure 9.** Interplate coupling and locations of intraplate strike-slip earthquakes on subduction zone. (a) Coupling distribution and locations of the  $M_w \geq 7.0$  intraplate strike-slip earthquakes on the Japan Trench (modified from [Graham et al., 2021](#)). (b) Coupling distribution and locations of the  $M_w \geq 7.0$  intraplate strike-slip earthquakes on the Ryukyu subduction zone (modified from [Graham et al., 2021](#)). (c) Schematic illustration of the interplate coupling and locations of intraplate strike-slip earthquakes in

Alaska. The gray dashed lines indicate the boundaries of the coupling changes—the interplate coupling information from [Li and Freymueller \(2018\)](#). The rupture regions of the 1938 and 1964 earthquakes are indicated by the dashed orange line according to [Benz et al. \(2011\)](#). The focal mechanisms from Global CMT of intraplate strike-slip earthquakes are plotted in red. The color version of this figure is available only in the electronic edition.

plate coupling in this region, we found that the refined rupture pattern of the 2020  $M_w$  7.6 strike-slip earthquake separated the boundaries of coupling rate of  $\sim 10\%$  to  $\sim 40\%$  (Fig. S8). The other  $M_w > 5.5$  intraplate strike-slip earthquakes since 1990 (Table S2) in this region were also located in areas with significant variations of plate coupling (Fig. 9c).

According to the offshore GPS observations, the subduction speed is varied from 63 mm/yr at Shumagin Island to 56 mm/yr at Kodiak Island along the Alaska–Aleutian subduction zone (Benz *et al.*, 2011). The different subducting speed of the downgoing plate would generate nearly trench-parallel tension stress environment, and prompt right-lateral strike-slip movement of trench-perpendicular fabrics (Herman and Furlong, 2021). The right-lateral slip of the trench-perpendicular fabrics would release the strain caused by the downgoing plate with nonuniform subducting speeds and thus likely cause the difference of the interplate coupling between both the sides of the strike-slip faults.

The correlation between the locations of intraplate strike-slip faults and variation of interplate coupling was also observed in the Japan trench and the Ryukyu subduction zone. We determined the orientations of the ruptured faults of the 2010  $M_w$  7.0 Ryukyu and the 2011  $M_w$  7.0 Honshu intraplate strike-slip earthquakes by back-projecting seismic data recorded at the U.S. stations (Fig. S9). The ruptured strike-slip faults in the two earthquakes well confined the boundaries of the coupling variations. The 2011  $M_w$  7.0 Honshu intraplate strike-slip earthquake occurred in the boundaries of the coupling rate of  $\sim 80\%$  to  $\sim 90\%$  (Fig. 9a), and the 2010  $M_w$  7.0 Ryukyu intraplate strike-slip earthquake occurred in the boundaries of the coupling of 0% to  $\sim 80\%$  (Fig. 9b; Graham *et al.*, 2021). Although we were not clear whether those strike-slip faults were linked to preexisting fabrics in the downgoing plate or were newly formed faults during the subducting process, their relations to the variation of the interplate coupling are evidently observed.

Therefore, we suggest that these structures within the subducting plate not only control the occurrence of intraplate earthquakes but also affect the interplate coupling. More importantly, intraplate earthquakes can be used to delineate the boundary of the coupling change. Hence, investigating preexisting fabrics is important for evaluating seismic hazards of future damaging intraplate earthquakes and understanding plate coupling information in subduction zones.

## Conclusions

Two-staged rupture migration of the 2020  $M_w$  7.6 Alaska earthquake was identified based on high-precision relocation of the earthquake sequence ( $M_w \geq 4.1$ ), back-projection analyses, and finite-fault modeling. The earthquake first ruptured southwestward  $\sim 16$  km along a steeply dipping fault plane (strike =  $15^\circ$ , dip =  $81^\circ$ ) for the initial 16 s and then propagated southeastward along a moderately dipping fault (strike =  $344^\circ$ ,

dip =  $48^\circ$ ) for the following  $\sim 10$  s. Considering the ruptured length of  $\sim 42$  km for the second portion, a fast speed of 4.2 km/s was obtained. Our two-staged rupture model can adequately explain the teleseismic observations. The strikes of the ruptured faults we obtained for the mainshock correlated well with the orientations of the linear magnetic anomalies. Therefore, the preexisting plate fabric in the subducted slab may act as the seismogenic faults of the intraplate strike-slip earthquakes.

In addition, the intraplate strike-slip earthquakes since 1990 in this region were located in areas with significant variations of plate coupling. Thus, preexisting plate fabric within the subducting plate may not only control the occurrence of intraplate strike-slip earthquakes but also affect the interplate coupling, which is critical for evaluating the seismic hazards of future megathrust earthquakes in subduction zones.

## Data and Resources

Global seismic data were obtained from the Incorporated Research Institutions for Seismology (<http://ds.iris.edu/ds>). The earthquake catalog is available online at the U.S. Geological Survey (<https://earthquake.usgs.gov/earthquakes>). The moment tensor solutions of the mainshock are available at Global Centroid Moment Tensor (<https://www.globalcmt.org/>). The LITHO1.0 model is available from the website <https://igppweb.ucsd.edu/~gabi/litho1.0.html>. The finite-fault model inversion code is MudPy (<https://github.com/dmelgarm/MudPy>) developed by Diego Melgar. Most figures were plotted using the software Generic Mapping Tools (<http://mirrors.ustc.edu.cn/gmt/>; Wessel and Smith, 1991). The seismic data recorded at Chinese stations are available at DOI: [10.5281/zenodo.6490101](https://doi.org/10.5281/zenodo.6490101) with free access. The supplemental material for this article includes 2 tables and 12 figures. All websites were last accessed in August 2021.

## Declaration of Competing Interests

The authors acknowledge that there are no conflicts of interest recorded.

## Acknowledgments

This research was supported by the National Key R&D Program of China (Number 2018YFC0603500) and the National Natural Science Foundation of China (NSFC) Grants 41874062 and 41922025. The authors also thank constructive suggestions and comments from Wei Wang (University of Southern California, California, United States) and Shanshan Li (Nanjing Tech University, Nanjing, China). The authors sincerely thank Editor-in-Chief Allison Bent, associate editor, and two anonymous reviewers for their constructive comments.

## References

- Atwater, T. (1989). Plate tectonic history of the northeast Pacific and western North America, in *The Eastern Pacific Ocean and Hawaii*, E. L. Winterer, D. M. Hussong, and R. W. Decker (Editors), Geological Society of America, Geology of North America, Boulder, Colorado, 21–72, doi: [10.1130/DNAG-GNA-N.21](https://doi.org/10.1130/DNAG-GNA-N.21).
- Benz, H. M., R. L. Dart, A. Villaseñor, G. P. Hayes, A. C. Tarr, K. P. Furlong, and S. Rhea (2011). Seismicity of the Earth 1900–2010

- Aleutian arc and vicinity, *U.S. Geol. Surv. Open-File Rept. 2010-1083-B*, scale 1:5000000, doi: [10.3133/ofr20101083B](https://doi.org/10.3133/ofr20101083B).
- Bull, J. M., and R. A. Scrutton (1990). Fault reactivation in the central Indian Ocean and the rheology of oceanic lithosphere, *Nature* **344**, no. 6269, 855–858, doi: [10.1038/344855a0](https://doi.org/10.1038/344855a0).
- Coxeter, H. S. M. (1969). *Introduction to Geometry*, Second Ed., Wiley Classics Library, New York City, New York, 289–290.
- Cross, R. S., and J. T. Freymueller (2008). Evidence for and implications of a Bering plate based on geodetic measurements from the Aleutians and western Alaska. *J. Geophys. Res.* **113**, no. B7, doi: [10.1029/2007JB005136](https://doi.org/10.1029/2007JB005136).
- Crowell, B. W., and D. Melgar (2020). Slipping the Shumagin gap: A kinematic coseismic and early afterslip model of the  $M_w$  7.8 Simeonof Island, Alaska, earthquake. *Geophys. Res. Lett.* **47**, no. 19, e2020GL090308, doi: [10.1029/2020GL090308](https://doi.org/10.1029/2020GL090308).
- Davies, J., L. Sykes, L. House, and K. Jacob (1981). Shumagin seismic gap, Alaska Peninsula: History of great earthquakes, tectonic setting, and evidence for high seismic potential, *J. Geophys. Res.* **86**, no. B5, 3821–3855, doi: [10.1029/JB086iB05p03821](https://doi.org/10.1029/JB086iB05p03821).
- Dziewonski, A. M., and D. L. Anderson (1981). Preliminary reference Earth model. *Phys. Earth Planet. In.* **25**, no. 4, 297–356, doi: [10.1016/0031-9201\(81\)90046-7](https://doi.org/10.1016/0031-9201(81)90046-7).
- Estabrook, C. H., and T. M. Boyd (1992). The Shumagin Islands, Alaska, earthquake of 31 May 1917, *Bull. Seismol. Soc. Am.* **82**, no. 2, 755–773, doi: [10.1785/BSSA0820020755](https://doi.org/10.1785/BSSA0820020755).
- Fan, W., and P. M. Shearer (2017). Investigation of backprojection uncertainties with M6 earthquakes, *J. Geophys. Res.* **122**, no. 10, 7966–7986, doi: [10.1002/2017JB014495](https://doi.org/10.1002/2017JB014495).
- Fletcher, H. J., J. Beavan, J. T. Freymueller, and L. Gilbert (2001). High interseismic coupling of the Alaska subduction zone SW of Kodiak island inferred from GPS data, *Geophys. Res. Lett.* **28**, no. 3, 443–446, doi: [10.1029/2000GL012258](https://doi.org/10.1029/2000GL012258).
- Fournier, T. J., and J. T. Freymueller (2007). Transition from locked to creeping subduction in the Shumagin region, Alaska, *Geophys. Res. Lett.* **34**, no. 6, L06303, doi: [10.1029/2006GL029073](https://doi.org/10.1029/2006GL029073).
- Graham, S. E., J. P. Loveless, and B. J. Meade (2021). A global set of subduction zone earthquake scenarios and recurrence intervals inferred from geodetically constrained block models of interseismic coupling distributions, *Geochem. Geophys. Geosys.* **22**, no. 11, e2021GC009802, doi: [10.1029/2021GC009802](https://doi.org/10.1029/2021GC009802).
- Guo, H., H. Zhang, R. M. Nadeau, and Z. Peng (2017). High-resolution deep tectonic tremor locations beneath the San Andreas fault near Cholame, California, using the double-pair double-difference location method, *J. Geophys. Res.* **122**, no. 4, 3062–3075, doi: [10.1002/2016JB013919](https://doi.org/10.1002/2016JB013919).
- Hansen, R. A., and N. A. Ratchkovski (2001). The Kodiak Island, Alaska  $M_w$  7 earthquake of 6 December 1999, *Seismol. Res. Lett.* **72**, no. 1, 22–32, doi: [10.1785/gssrl.72.1.22](https://doi.org/10.1785/gssrl.72.1.22).
- Hardebeck, J. L., and P. M. Shearer (2002). A new method for determining first-motion focal mechanisms, *Bull. Seismol. Soc. Am.* **92**, no. 6, 2264–2276, doi: [10.1785/0120010200](https://doi.org/10.1785/0120010200).
- Hayes, G. P., G. L. Moore, D. E. Portner, M. Hearne, H. Flamme, M. Furtney, and G. M. Smoczyk (2018). Slab2, a comprehensive subduction zone geometry model. *Science* **362**, no. 6410, 58–61, doi: [10.1126/science.aat4723](https://doi.org/10.1126/science.aat4723).
- Huang, X., Y. Peng, C. Cheng, D. Wang, and Q. Yao (2022). Determination and comparison of  $M_L$ ,  $M_S$ ,  $m_B$ ,  $M_{wp}$ ,  $M_{ww}$ ,  $M_{dt}$ , and  $M$  (GNSS) for the 22 May 2021  $M7.4$  Madoi, Qianghai, China earthquake, *J. Earth Sci.* **33**, no. 4, 847–856, doi: [10.1007/s12583-022-1680-7](https://doi.org/10.1007/s12583-022-1680-7).
- Herman, M. W., and K. P. Furlong (2021). Triggering an unexpected earthquake in an uncoupled subduction zone, *Sci. Adv.* **7**, no. 13, doi: [10.1126/sciadv.abf7590](https://doi.org/10.1126/sciadv.abf7590).
- Herman, M. W., R. B. Herrmann, H. M. Benz, and K. P. Furlong (2014). Using regional moment tensors to constrain the kinematics and stress evolution of the 2010–2013 Canterbury earthquake sequence, South Island, New Zealand, *Tectonophysics* **633**, no. 21, 1–15, doi: [10.1016/j.tecto.2014.06.019](https://doi.org/10.1016/j.tecto.2014.06.019).
- Ishii, M., P. M. Shearer, H. Houston, and J. E. Vidale (2005). Extent, duration and speed of the 2004 Sumatra-Andaman earthquake imaged by the Hi-Net array, *Nature* **435**, 933–936, doi: [10.1038/nature03675](https://doi.org/10.1038/nature03675).
- Jacob, J., J. Dymant, D. Ghosal, and P. Dewangan (2021). Strike-slip seismicity at the Andaman-Sumatra subduction zone: Role of the fracture zones and age of the subducting lithosphere, *Tectonophysics* **811**, doi: [10.1016/j.tecto.2021.228862](https://doi.org/10.1016/j.tecto.2021.228862).
- Jiang, Y., P. J. González, and R. Bürgmann (2022). Subduction earthquakes controlled by incoming plate geometry: The 2020  $M > 7.5$  Shumagin, Alaska, earthquake doublet, *Earth Planet. Sci. Lett.* **584**, doi: [10.1016/j.epsl.2022.117447](https://doi.org/10.1016/j.epsl.2022.117447).
- Karner, G. D., N. W. Driscoll, and J. K. Weisell (1993). Response of the lithosphere to in-plane force variations, *Earth Planet. Sci. Lett.* **114**, no. 4, 397–416, doi: [10.1016/0012-821X\(93\)90072-H](https://doi.org/10.1016/0012-821X(93)90072-H).
- Kennett, B. L. N., and E. R. Engdahl (1991). Traveltimes for global earthquake location and phase identification, *Geophys. J. Int.* **105**, no. 2, 429–465, doi: [10.1111/j.1365-246X.1991.tb06724.x](https://doi.org/10.1111/j.1365-246X.1991.tb06724.x).
- Kiser, E., and M. Ishii (2012). Combining seismic arrays to image the high-frequency characteristics of large earthquakes, *Geophys. J. Int.* **188**, no. 3, 1117–1128, doi: [10.1111/j.1365-246X.2011.05299.x](https://doi.org/10.1111/j.1365-246X.2011.05299.x).
- Koper, K. D., A. R. Hutko, T. Lay, and O. Sufri (2012). Imaging short-period seismic radiation from the 27 February 2010 Chile ( $M_w$  8.8) earthquake by back-projection of P, PP, and PKIKP waves, *J. Geophys. Res.* **117**, no. B2, doi: [10.1029/2011JB008576](https://doi.org/10.1029/2011JB008576).
- Krabbenhoft, A., R. von Huene, J. J. Miller, and D. Klaeschen (2021). Subducting oceanic basement roughness impacts on upper plate tectonic structure and a backstop splay fault zone activated in the southern Kodiak aftershock region of the  $M_w$  9.2, 1964 megathrust rupture, Alaska, *Geospheres* **17**, no. 2, 409–437, doi: [10.1130/GES02275.1](https://doi.org/10.1130/GES02275.1).
- Krabbenhoft, A., R. von Huene, J. J. Miller, D. Lange, and F. Vera (2018). Strike-slip 23 January 2018  $M_w$  7.9 Gulf of Alaska rare intraplate earthquake: Complex rupture of a fracture zone system, *Sci. Rep.* **8**, no. 1, 1–9, doi: [10.1038/s41598-018-32071-4](https://doi.org/10.1038/s41598-018-32071-4).
- Lawson, C. L., and R. J. Hanson (1995). *Solving Least Squares Problems[M]*, Society for Industrial and Applied Mathematics. Prentice-Hall, Englewood Cliffs, New Jersey.
- Li, Q., B. Zhao, K. Tan, and W. B. Xu (2020). Two main rupture stages during the 2018 magnitude 7.5 Sulawesi earthquake, *Geophys. J. Int.* **221**, no. 3, 1873–1882, doi: [10.1093/gji/ggaa115](https://doi.org/10.1093/gji/ggaa115).
- Li, S., and J. T. Freymueller (2018). Spatial variation of slip behavior beneath the Alaska Peninsula along Alaska-Aleutian subduction zone, *Geophys. Res. Lett.* **45**, no. 8, 3453–3460, doi: [10.1002/2017GL076761](https://doi.org/10.1002/2017GL076761).

- Liu, C. L., T. Lay, X. Xiong, and Y. M. Wen (2020). Rupture of the 2020  $M_w$  7.8 earthquake in the Shumagin gap inferred from seismic and geodetic observations. *Geophys. Res. Lett.* **47**, no. 22, 1–9, doi: [10.1029/2020GL090806](https://doi.org/10.1029/2020GL090806).
- Meng, L., J. P. Ampuero, J. Stock, Z. Duputel, Y. Luo, and V. C. Tsai (2012). Earthquake in a maze: Compressional rupture branching during the 2012  $M_w$  8.6 Sumatra earthquake. *Science* **337**, no. 6095, 724–726, doi: [10.1126/science.1224030](https://doi.org/10.1126/science.1224030).
- Naugler, F. P., and J. M. Wageman (1973). Gulf of Alaska: Magnetic anomalies, fracture zones, and plate interaction. *Geol. Soc. Am. Bull.* **84**, no. 5, 1575–1584.
- Pasyanos, M. E., T. G. Masters, G. Laske, and Z. Ma (2014). LITHO1.0: An updated crust and lithospheric model of the Earth. *J. Geophys. Res.* **119**, 2153–2173, doi: [10.1002/2013JB010626](https://doi.org/10.1002/2013JB010626).
- Ratchkovski, N. A., and R. A. Hansen (2001). Sequence of strong intraplate earthquakes in the Kodiak Island region, Alaska in 1999–2001. *Geophys. Res. Lett.* **28**, no. 19, 3729–3732, doi: [10.1029/2001GL013416](https://doi.org/10.1029/2001GL013416).
- Saffer, D. M., and H. J. Tobin (2011). Hydrogeology and mechanics of subduction zone forearcs: Fluid flow and pore pressure. *Annu. Rev. Earth Planet. Sci.* **39**, 157–186, doi: [10.1146/annurev-earth-040610-133408](https://doi.org/10.1146/annurev-earth-040610-133408).
- Satriano, C., E. Kiraly, P. Bernard, and J.-P. Vilotte (2012). The 2012  $M_w$  8.6 Sumatra earthquake: Evidence of westward sequential seismic ruptures associated to the reactivation of a N-S ocean fabric. *Geophys. Res. Lett.* **39**, no. 15, doi: [10.1029/2012GL052387](https://doi.org/10.1029/2012GL052387).
- Shillington, D. J., A. Bécel, and M. R. Nedimović (2020). Upper plate structure and megathrust properties in the Shumagin gap near the July 2020  $M_w$  7.8 Simeonof event. *Geophys. Res. Lett.* **49**, no. 2, doi: [10.1029/2021GL096974](https://doi.org/10.1029/2021GL096974).
- Song, C., Q. Yao, and D. Wang (2019). Magnitude of the 23 January 2018  $M_w$  7.9 Alaska earthquake estimated from local dense seismic records in Alaska. *J. Earth Sci.* **30**, no. 5, 1005–1009, doi: [10.1007/s12583-019-1215-z](https://doi.org/10.1007/s12583-019-1215-z).
- Sun, T., S. Ellis, and D. Saffer (2020). Coupled evolution of deformation, pore fluid pressure, and fluid flow in shallow subduction forearcs. *J. Geophys. Res.* **125**, no. 3, doi: [10.1029/2019JB019101](https://doi.org/10.1029/2019JB019101).
- Sykes, L. R. (1971). Aftershock zones of great earthquakes, seismicity gaps, and earthquake prediction for Alaska and the Aleutians. *J. Geophys. Res.* **76**, no. 32, 8021–8041, doi: [10.1029/JB076i032p08021](https://doi.org/10.1029/JB076i032p08021).
- Tsuji, T., S. Minato, R. Kamei, T. Tsuru, and G. Kimura (2017). 3D geometry of a plate boundary fault related to the 2016 off-Mie earthquake in the Nankai subduction zone, Japan. *Earth Planet. Sci. Lett.* **478**, 234–244, doi: [10.1016/j.epsl.2017.08.041](https://doi.org/10.1016/j.epsl.2017.08.041).
- Valenzuela, R. W., and M. E. Wysession (1993). Intraplate earthquakes in the southwest Pacific Ocean basin and the seismotectonics of the southern Tasman Sea. *Geophys. Res. Lett.* **20**, no. 22, 2467–2470, doi: [10.1029/93GL02792](https://doi.org/10.1029/93GL02792).
- Vallée, M., and C. Satriano (2014). Ten year recurrence time between two major earthquakes affecting the same fault segment. *Geophys. Res. Lett.* **41**, no. 7, 2312–2318, doi: [10.1002/2014GL059465](https://doi.org/10.1002/2014GL059465).
- Wang, D., and A. R. Hutko (2018). Relative relocations of the North Korean nuclear tests from 2006 to 2017 using the Hi-net array in Japan. *Geophys. Res. Lett.* **45**, no. 15, 7481–7487, doi: [10.1029/2018GL078653](https://doi.org/10.1029/2018GL078653).
- Wang, D., and J. Mori (2012). The 2010 Qinghai, China, earthquake: A moderate earthquake with supershear rupture. *Bull. Seismol. Soc. Am.* **102**, no. 1, 301–308, doi: [10.1785/0120110034](https://doi.org/10.1785/0120110034).
- Wang, D., Y. Chen, Q. Wang, and J. Mori (2018). Complex rupture of the 13 November 2016  $M_w$  7.8 Kaikoura, New Zealand earthquake: Comparison of high-frequency and low-frequency observations. *Tectonophysics* **733**, 100–107, doi: [10.1016/j.tecto.2018.02.004](https://doi.org/10.1016/j.tecto.2018.02.004).
- Wang, D., J. Mori, and T. Uchide (2012). Supershear rupture on multiple faults for the  $M_w$  8.6 off northern Sumatra, Indonesia earthquake of April 11, 2012. *Geophys. Res. Lett.* **39**, no. 21, doi: [10.1029/2012GL053622](https://doi.org/10.1029/2012GL053622).
- Wang, R., S. Heimann, Y. Zhang, H. Wang, and T. Dahm (2017). Complete synthetic seismograms based on a spherical self-gravitating Earth model with an atmosphere–ocean–mantle–core structure. *Geophys. J. Int.* **210**, no. 3, 1739–1764, doi: [10.1093/gji/ggx259](https://doi.org/10.1093/gji/ggx259).
- Weissel, J. K., R. N. Anderson, and C. A. Geller (1980). Deformation of the Indo-Australian plate. *Nature* **287**, no. 5780, 284–291, doi: [10.1038/287284a0](https://doi.org/10.1038/287284a0).
- Wessel, P., and W. H. Smith (1991). Free software helps map and display data. *Eos Trans. AGU* **72**, no. 41, 441–446, doi: [10.1029/90EO00319](https://doi.org/10.1029/90EO00319).
- Xiao, L., R. Zheng, and R. Zou (2022). Coseismic slip distribution of the 2021  $M_w$  7.4 Maduo, Qinghai earthquake estimated from InSAR and GPS measurements. *J. Earth Sci.* **33**, no. 4, 885–891, doi: [10.1007/s12583-022-1637-x](https://doi.org/10.1007/s12583-022-1637-x).
- Yao, H., P. M. Shearer, and P. Gerstoft (2012). Subevent location and rupture imaging using iterative backprojection for the 2011 Tohoku  $M_w$  9.0 earthquake. *Geophys. J. Int.* **190**, no. 2, 1152–1168, doi: [10.1111/j.1365-246X.2012.05541.x](https://doi.org/10.1111/j.1365-246X.2012.05541.x).
- Ye, L. L., T. Lay, H. Kanamori, Y. Yamazaki, and K. F. Cheung (2021). The 22 July 2020  $M_w$  7.8 Shumagin seismic gap earthquake: Partial rupture of a weakly coupled megathrust. *Earth Planet. Sci. Lett.* **562**, no. 15, doi: [10.1016/j.epsl.2021.116879](https://doi.org/10.1016/j.epsl.2021.116879).
- Yokota, Y., T. Ishikawa, S. I. Watanabe, T. Tashiro, and A. Asada (2016). Seafloor geodetic constraints on interplate coupling of the Nankai trough megathrust zone. *Nature* **534**, no. 7607, 374–377, doi: [10.1038/nature17632](https://doi.org/10.1038/nature17632).
- Zhang, H., and Z. Ge (2010). Tracking the rupture of the 2008 Wenchuan earthquake by using the relative back-projection method. *Bull. Seismol. Soc. Am.* **100**, no. 5B, 2551–2560, doi: [10.1785/0120090243](https://doi.org/10.1785/0120090243).
- Zhao, L. F., X. B. Xie, W. M. Wang, J. L. Hao, and Z. X. Yao (2016). Seismological investigation of the 2016 January 6 North Korean underground nuclear test. *Geophys. J. Int.* **206**, no. 3, 1487–1491, doi: [10.1093/gji/ggw239](https://doi.org/10.1093/gji/ggw239).
- Zheng, X. F., Z. X. Yao, J. H. Liang, and J. Zheng (2010). The role played and opportunities provided by IGP DMC of China National Seismic Network in Wenchuan earthquake disaster relief and researches. *Bull. Seismol. Soc. Am.* **100**, no. 5B, 2866–2872, doi: [10.1785/0120090257](https://doi.org/10.1785/0120090257).
- Zhou, Y., W. Wang, J. He, X. Wang, Z. Pan, and G. Zhao (2022). The 19 October 2020  $M_w$  7.6 earthquake in Shumagin, Alaska: An unusual dextral strike-slip event. *Pure Appl. Geophys.* doi: [10.1007/s00024-022-03001-3](https://doi.org/10.1007/s00024-022-03001-3).